Ray tracing the Wigner distribution function for optical simulations

Mout, Marco; Wick, Michael; Bociort, Florian; Petschulat, Joerg; Urbach, Paul

Optical Engineering

Ray tracing the Wigner distribution function for optical simulations

Marco Mout
Michael Wick
Florian Bociort
Joerg Petschulat
Paul Urbach

Ray tracing the Wigner distribution function for optical simulations

Marco Mout,[a,b,][*] **Michael Wick,**[c] **Florian Bociort,**[b] **Joerg Petschulat,**[a] **and Paul Urbach**[b]
[a]Carl Zeiss AG, Oberkochen, Germany
[b]Delft University of Technology, Department of Imaging Physics, Delft, The Netherlands
[c]Coburg University of Applied Sciences, Coburg, Germany

Abstract. We study a simulation method that uses the Wigner distribution function to incorporate wave optical effects in an established framework based on geometrical optics, i.e., a ray tracing engine. We use the method to calculate point spread functions and show that it is accurate for paraxial systems but produces unphysical results in the presence of aberrations. The cause of these anomalies is explained using an analytical model. © 2018 Society of Photo-Optical Instrumentation Engineers (SPIE) [DOI: 10.1117/1.OE.57.1.014106]

1 Introduction

The consideration of multiple diffraction and field propagation becomes increasingly important due to the application in devices, such as head-up displays and head-mounted displays, where diffraction and aberrations have to be precisely accounted for in order to achieve optical designs with the required visual quality. Knowledge of these ray-based propagation methods and their limits can be of crucial importance in the development of such devices.

Several methods that describe diffraction phenomena by means of ray tracing exist (e.g., Refs. 1–4). They can be powerful tools, in particular for simulating multiple diffraction or field propagation in the presence of aberrations. However, every method involves approximations and has a limited domain of applicability. Here, we report on the approximations and limits of a ray-based simulation method that uses the Wigner distribution function (WDF) to incorporate the effects of diffraction for monochromatic fully spatially coherent fields.

The WDF is a bilinear transformation of a complex function, introduced in 1932 by Wigner.[5] Its definition is

$$W(\boldsymbol{x}, \boldsymbol{\xi}) = \iint E\left(\boldsymbol{x} + \frac{\boldsymbol{x}'}{2}\right) E^*\left(\boldsymbol{x} - \frac{\boldsymbol{x}'}{2}\right) e^{-i\boldsymbol{\xi}\cdot\boldsymbol{x}'} d^2\boldsymbol{x}', \qquad (1)$$

where W is the WDF, $\boldsymbol{x} = (x_1, x_2)$ represents a point in a plane in ordinary space, $\boldsymbol{\xi} = (\xi_1, \xi_2)$ is a point in reciprocal space, E is a monochromatic scalar complex field, and the integral is over the auxiliary coordinates $d^2\boldsymbol{x}' = dx_1' dx_2'$. The WDF is always real but not necessarily positive (see, e.g., Ref. 6). When used in optics, the WDF can serve as a representation of the scalar electric field, E. Such a representation was first introduced by Dolin[7] and later again by Walther.[8] When describing the electric field using the WDF, the frequency marginal of the WDF gives the spatial intensity distribution, and the spatial marginal gives the intensity of the plane wave expansion of the field:[9]

$$I(\boldsymbol{x}) = \frac{1}{(2\pi)^2} \iint W(\boldsymbol{x}, \boldsymbol{\xi}) d^2\boldsymbol{\xi}, \qquad (2)$$

$$|\tilde{E}(\boldsymbol{\xi})|^2 = \iint W(\boldsymbol{x}, \boldsymbol{\xi}) d^2\boldsymbol{x}. \qquad (3)$$

If a field E is propagated through an optical system using paraxial optics, the corresponding WDF changes by a mere coordinate transformation. The effect of propagating the field, in the paraxial regime through a homogenous medium over a distance z, is, for instance, given by

$$W_z(\boldsymbol{x}, \boldsymbol{\xi}) = W_0\left(\boldsymbol{x} - \frac{\boldsymbol{\xi}}{k}z, \boldsymbol{\xi}\right), \qquad (4)$$

where k is the wavenumber of the light in the medium. This coordinate transformation is identical to the one that describes the change in position and direction of a geometrical optical ray, with directional cosines given by

$$p_j = \frac{\xi_j}{k}, \qquad (5)$$

where the index j indicates the first or second element of a vector. The coordinate transformations of the WDF and geometrical optics are also identical for the propagation through a paraxial lens or a paraxial system of lenses and free-space.[9] For a more detailed treatment of these and other properties of the WDF, the reader is referred to one of the early papers on the WDF in optics[9] and an extensive tutorial.[6]

Because the coordinate transformations of the WDF and of paraxial rays are identical, the WDF remains constant along paths followed by paraxial rays. To the knowledge of the authors, the first usage of this property for ray-based diffraction simulation was in the field of computer graphics.[10] Oh et al. rendered images that showed diffraction patterns, e.g., of a light source behind a square aperture casting a diffraction pattern on a cubic box. They also computed

---

point spread functions (PSFs) for two camera lenses with different numerical apertures (NAs).[10] Although some of the diffraction patterns were validated using Fourier optics, the PSFs were only evaluated qualitatively. The method by Oh et al. was further developed in the computer graphics community (e.g., Refs. 11–13), but PSF calculations were never validated.

The aim of this paper is to assess such a ray-based transport of the WDF for optical simulations. We will discuss its potential and evaluate its limitations by comparing the results to those of reference methods. The focus will be on the simulation of the propagation of monochromatic spatially coherent scalar electric fields through optical systems.

2 Method

The principles described in Refs. 10–13 are implemented in a simulation method, which we call Wigner-based ray tracing (WBRT). The aim of WBRT is to simulate the propagation of an electric field from an input plane, through an optical system consisting of, e.g., free-space, lenses, and apertures, and calculate the intensity distribution at an output plane. We first presented this method in a preliminary form in 2015.[14] A simulation consists of several steps, which are illustrated in the flowchart in Fig. 1 and described in the following paragraphs.

The first step of WBRT is to derive the WDF of the electric field in the input plane. For some frequently used input fields, the WDF can be calculated analytically. The WDF of a plane wave with amplitude A and a wave vector, whose components parallel to the reciprocal plane are $\boldsymbol{k} = (k_x, k_y)$, is, for instance, given by

$$W(\boldsymbol{x}, \boldsymbol{\xi}) = (2\pi)^2 |A|^2 \delta(\boldsymbol{\xi} - \boldsymbol{k}). \tag{6}$$

WBRT performs a Monte Carlo sampling of the region of the four-dimensional phase space for which $W(\boldsymbol{x}, \boldsymbol{\xi}) \neq 0$. The algorithm chooses a (user defined) number of random points within this region of phase space, using a probability distribution function that is uniform in spatial and frequency coordinates. Every such point in phase space is associated with a ray with the same spatial coordinates $\boldsymbol{x}$ and directions defined by Eq. (5) that carries the local WDF.

The second step is to use these rays to propagate the WDF through an optical system, e.g., a series of lenses in free-space. The lenses will affect the ray paths according to Snell's law but will not introduce diffraction unless they are combined with an aperture. Within the paraxial theory this procedure is exact, since the WDF remains constant along the paths of paraxial rays. The underlying assumption of WBRT is that this property is also a good approximation beyond the paraxial domain.

At an aperture or (complex) mask, the ray tracing is interrupted. In WBRT, masks are treated within the thin element approximation. As a result, the effect of a mask on the electric field is given by

$$E_{\mathrm{o}}(\boldsymbol{x}) = B(\boldsymbol{x})E_{\mathrm{in}}(\boldsymbol{x}), \tag{7}$$

where the indices "in" and "o" indicate the input and the output, and $B(\boldsymbol{x})$ is the complex mask function. By using Eq. (1) and its inverse on Eq. (7), one can derive

$$W_{\mathrm{o}}(\boldsymbol{x}, \boldsymbol{\eta}) = \frac{1}{(2\pi)^2} \iint W_{\mathrm{in}}(\boldsymbol{x}, \boldsymbol{\xi}) W_B(\boldsymbol{x}, \boldsymbol{\eta} - \boldsymbol{\xi}) \mathrm{d}^2\boldsymbol{\xi}. \tag{8}$$

This means that the WDF directly after a mask can be calculated by a convolution of the input WDF (W_{in}) with the WDF of the mask (W_B) over the frequency variables.[9] Since the mask function can be complex, it can be used to describe aberrations within the thin element approximation. Such a procedure has, for instance, been used to study the effect of aberrations in the exit pupil[15] but requires an additional (ray-based) method to calculate the aberrations. In WBRT, aberrations are implicitly captured by the ray tracing procedure, whereas diffraction is explicitly introduced by convolving the WDF of the field and the aperture function. Note that as a result of this convolution, the WDF is smeared out over the frequency variables but remains localized in spatial coordinates. In our ray-based model, this is implemented by letting every ray initiate a set of new rays. These rays have the same initial position but differ in directions and carry a value of the WDF in accordance with Eq. (8). The set of secondary rays is created using a Monte Carlo procedure similar to the one used for the creation of the initial rays. This follows the example of the work by Oh et al.[10] and makes the method very suited for parallel computing. In this paper, we treat apertures using the Kirchhoff boundary conditions.[16] Therefore, the mask function $B(\boldsymbol{x})$ reduces to a binary function with the value 1 inside and 0 outside of the aperture. The WDF of a square aperture can be calculated analytically and the result is given later in this paper. For the WDF of circular apertures, Bastiaans derived a simplified integral equation. [17]

Further propagation through the optical system is again carried out using ray tracing, and further apertures can be treated in accordance with Eq. (8).

As a final step, the intensity distribution at the output plane (or any other plane) is calculated. Since the intensity distribution is given by the frequency marginal of the WDF [see Eq. (2)], the intensity in a pixel can be calculated by summing the values of the WDF carried by each ray that hits the pixel. Using these principles, one can obtain an intensity distribution in a plane caused by the propagation of a coherent field through an optical system.
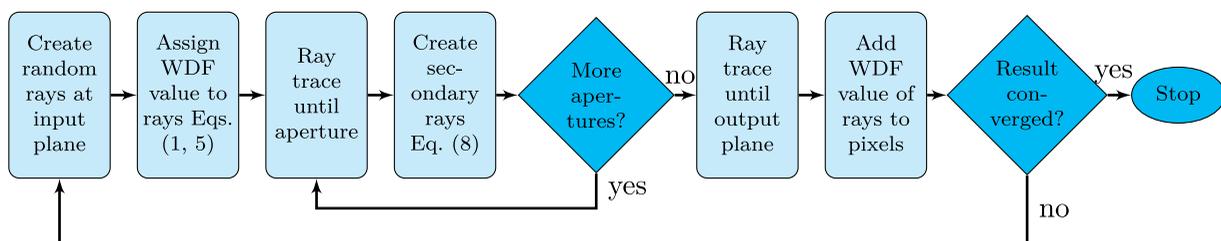
Fig. 1 A flowchart illustrating the steps of WBRT.

3 Results

The procedure described in the previous section is implemented in MATLAB and used to simulate the propagation of a plane wave, through a thick and thin lens, for wavefronts with and without aberrations.

3.1 Thick Lens

The results of the propagation of a plane wave through a thick lens are shown in Figs. 2 and 3. Apart from the WBRT results, the figures also show the results of a Rayleigh–Sommerfeld exit pupil diffraction integral (RSED)[18] obtained with an in-house optical simulation software package. Figure 2 shows the results for axial imaging by a singlet with an NA of 0.2 that introduces no third or fifth order spherical aberrations to the wavefront. The results from WBRT and RSED are in very good agreement. For the other singlet, which has an NA of 0.04, and wavefront aberrations with root mean square (rms) values of 0.23

wavelengths for defocus and 0.12 wavelengths for primary spherical aberrations, WBRT results in negative intensities, which is clearly unphysical. It also indicates that WBRT results in a distribution other than the WDF, since the marginals of the WDF are always nonnegative (see, e.g., Ref. 6).

These results indicate that the validity of WBRT mainly depends on the wavefront aberrations. This is further supported by Figs. 4 and 5, where the agreement between the WBRT and RSED simulation is quantified in the L2-difference of the simulated PSFs, defined by

$$L_2 = \sqrt{\frac{\sum_p [A'(p) - A(p)]^2}{\sum_p A'(p)^2}}, \qquad (9)$$

where $A'(p)$ is the amplitude at pixel p predicted by the RSED and $A(p)$ is the corresponding amplitude given by WBRT. The figures show the results for one spherical and three aspherical singlets with varying aperture radii. For

Fig. 2 Cross-section of the PSF of a singlet at a wavelength of 600 nm calculated using WBRT and the RSED. The system has an NA of 0.2 and an aperture radius of 100 mm and produces a wavefront free of noticeable aberrations. The results from WBRT are averaged over the polar angle. The convergence is better at larger distances from the origin, because the average there is taken over a larger number of Monte Carlo samples. Near the origin one can notice the statistical noise due to the lower Monte Carlo sampling.

Fig. 4 The L2-difference between WBRT and RSED simulations of four lens designs at varying aperture radii. All systems consist of a singlet followed by a circular aperture and a free-space propagation over 500 mm. The systems are illuminated at 600 nm by a plane wave or a point source 800 mm in front of the lens (asphere B). The error increases sharply at aperture radii of around 10, 90, and 120 mm, respectively.

Fig. 3 Cross-section of the PSF of a singlet at a wavelength of 600 nm, calculated using WBRT and the RSED. The aperture has a radius of 20 mm and the system has an NA of 0.04. The main aberrations are defocus and spherical aberrations. The results from WBRT show unphysical negative intensities.
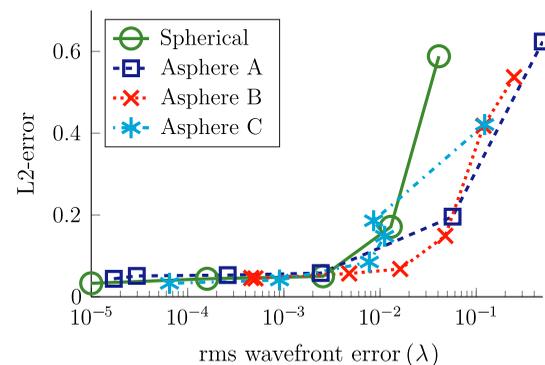
Fig. 5 The L2-difference between WBRT and RSED simulations of the four lens designs used in Fig. 4 simulated at the same aperture radii as for Fig. 4. The horizontal axis shows the rms wavefront error (excluding tip/tilt and defocus). For all four systems, the L2-difference starts to increase significantly for rms wavefront errors onward of 10^{-2} wavelength.

these singlets, the radius at which the WBRT and RSED results start to diverge (see Fig. 4) varies between 10 and 120 mm, corresponding to NAs of 0.02 and 0.23. In Fig. 5, the same results are plotted but with the rms wavefront error (excluding tip/tilt and defocus) instead of the aperture radius on the horizontal axis. From rms wavefront errors of around 10^{-2} wavelength onward, the L2-difference between the WBRT and RSED results starts to increase for all four singlets. Although the exact rms wavefront error at which this occurs is different for every system, simulations at different NAs and for different spherical and aspherical singlets show similar results: the results of WBRT and the RSED are in good agreement until spherical aberrations start influencing the PSF. Unless future research finds a way to solve this difficulty with an approach that differs significantly from the present one, it is safer not to use WBRT for thick lenses that suffer from aberrations.

Other simulations show that for systems with very small aberrations and NAs larger than 0.3, the results from WBRT and RSED also diverge, indicating the limits of WBRT due to nonparaxial effects. For the aberration-free wavefronts, we did not encounter negative intensities.

3.2 Thin Lens

To study the effects of aberrations on WBRT, the simulation of a singlet was repeated using a thin-element model. Within the thin-element approximation, all effects of the lens (i.e., phase changes or changes in ray direction) occur in a plane. The effect of a thin lens that introduces aberrations can be modeled by two separate stages. First, the lens will change the direction of each ray in accordance with perfect imaging. Second, the aberrations will cause small additional directional changes of the rays.

The results of the thin-lens model, for a lens that introduces aberrations and a lens that does not, are shown in Fig. 6. The Airy pattern, which is plotted as a reference, and the result for the thin lens in the aberration-free case, are in very good agreement. Note that the thin lens has an NA of 0.45. When spherical aberration is introduced, WBRT gives unphysical results in the form of spatial regions with a negative intensity.
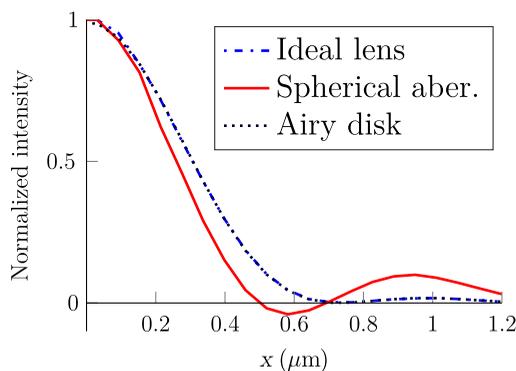
Fig. 6 Cross-section of the PSF of an ideal thin lens and a thin lens that introduces spherical aberrations calculated using WBRT. The lenses have an NA of 0.45, an aperture radius of 10 mm, and the wavelength is 600 nm. The result of the ideal thin lens is in good agreement with the corresponding Airy disk.

3.3 Analytical Model

These results suggest that the negative intensities observed in WBRT simulations are the effect of an inaccurate model of aberrations. In order to rule out other causes, e.g., inadequate sampling, we investigate an analytical model based on WBRT.

The analytical model is derived for the simplified case of a thin lens with only one spatial dimension perpendicular to the optical axis. The WDF of the one-dimensional plane wave that is incident on the lens is given by

$$W_1(x_1, \xi_1) = 2\pi\delta(\xi_1 - k_x). \tag{10}$$

The one-dimensional aperture is a slit of width $2w$ with a WDF of

$$W_B(x, \xi) = \begin{cases} \frac{2}{\xi}\sin[\xi 2(w - |x|)] & \text{if } |x| \leq w \\ 0 & \text{if } |x| > w \end{cases}. \tag{11}$$

The result of the convolution [see Eq. (8)] between these two WDFs is

$$W_2(x_2, \xi_2) = \begin{cases} \frac{2\sin[(\xi_2 - k_x)2(w - |x_2|)]}{\xi_2 - k_x} & \text{if } |x_2| \leq w \\ 0 & \text{if } |x_2| > w \end{cases}. \tag{12}$$

The propagation through the thin (aberrated) lens to the image plane is treated in two steps. First, the effect of the aberrations is modeled by a coordinate transformation of the ray direction:

$$W_3(x_3, \xi_3) = W_2[x_3, \xi_3 - f(x_3, k_x)], \tag{13}$$

where the function f, in accordance with geometrical optics, is the derivative of the wavefront aberration with respect to the spatial pupil coordinate (x_3). For spherical aberration, this is $f(x_3, k_x) = ax_3^3$, with a a constant. The rest of the system can now be considered to be an ideal imaging system, which maps a spatial frequency in the pupil plane (ξ_3) to a position in the image plane (x_i). Characterizing this mapping by a magnification factor M, the intensity in the image plane is given by

$$I(x_i) = \int W_3(x_3, x_i/M)dx_3, \tag{14}$$

$$= \int_{-w}^{w} \sin\left\{\left[\frac{x_i}{M} - f(x_3, k_x) - k_x\right]2(w - |x_3|)\right\}, \frac{2}{\frac{x_i}{M} - f(x_3, k_x) - k_x}dx_3. \tag{15}$$

For the aberration-free case, this results in the sinc [$\text{sinc}(t) \equiv \sin(t)/t$] pattern, familiar from the Fraunhofer diffraction pattern of a square aperture:[19]

$$I(x_i) = 4w^2 \text{sinc}^2[(x_i/M - k_x)w]. \tag{16}$$

In the case of aberrations, an analytical evaluation of Eq. (15) is nontrivial. A numerical evaluation of the integral, using the integral function of MATLAB, for different types of aberrations is shown in Fig. 7, along with the result for the aberration-free imaging. Negative intensities can be observed
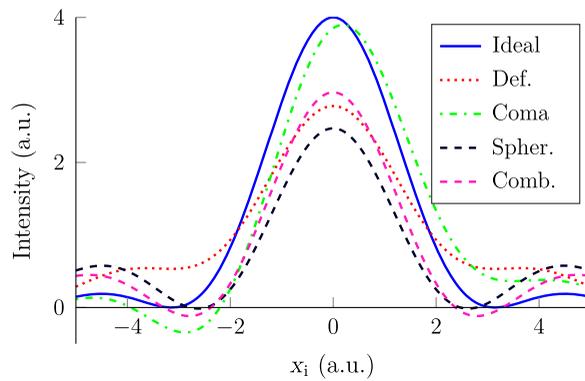
Fig. 7 Numerical solutions of Eq. (15) for different aberrations. The half-width of the slit, w, and the magnification factor, M, are set to one. Both the result for coma and spherical aberrations (Spher.) show negative intensities, although the minimum intensity for spherical aberrations is only −0.02. When adding some defocus to the spherical aberration (Comb.), the negativity is more pronounced. The result for the ideal lens corresponds to Eq. (16). Intensity patterns for the ideal lens were calculated for a wide range of defoci. All these defocused intensity patterns were strictly positive. The figure shows one typical result (Def.).

for spherical aberration and coma, whereas the results for the ideal and defocused systems remain strictly positive.

The fact that the analytical model reproduces the effects observed in the other WBRT simulations shows that the unphysical results are inherent to the underlying model of WBRT and not related to the (numerical) implementation of the method. In simulations over a wide range of NAs, the negative intensities were only encountered in the presence of aberrations. It therefore appears that, specifically, the model of aberrations in WBRT is inaccurate.

4 Discussion

The negative intensities observed in WBRT can be explained by the simplified model of aberrations. In the thin element approximation, aberrations can be introduced using a phase mask and Eq. (7). The effect on the WDF is a convolution between the WDF of the phase mask and the input field [Eq. (8)]. The WDF of a function with a complex quadratic exponent, e.g., the quadratic phase function of defocus, reduces to a (double) delta function. As a result, the effect on the WDF of, e.g., defocus is a coordinate transformation. This coordinate transformation is implicitly implemented in WBRT by ray tracing and explicitly introduced in the analytical model by Eq. (13). However, coma and spherical aberration have third and fourth order phase functions. It was shown by Lohmann et al.,[20] that the effect of such aberrations in the exit pupil on the WDF is twofold. First, they lead to a coordinate transformation in accordance with geometrical optics [Eq. (13)], and second, they lead to differential operators that change the shape of the WDF. For a cubic phase function, this results in a WDF concentrated around a second order function but blurred by the Airy integral.[21] In WBRT, the coordinate transformation is implemented, but the blurring by the differential operators is neglected. Our results show that for the simulation of PSFs, this second effect is of crucial importance. But, since in WBRT, a ray only carries the local value of the WDF, one cannot apply the differential operators on the individual samples but must first rebuild the entire WDF. This would complicate the model and increase

the computational load of WBRT to a great extent. Furthermore, an additional simulation method would be needed to calculate the aberrations. Some WDF simulations might benefit from modeling aberrations by coordinate transformations and differential operators or by a direct convolution with a WDF describing the aberrations, but we consider it infeasible for WBRT due to the above-mentioned reasons. Contrary to hopes expressed elsewhere in the literature,[13,22] our results show that it is insufficient to model aberrations by mere coordinate transformations of the WDF.

Although WBRT is unsuited for systems with aberrations, it can be used for modeling aberration-free systems with moderate NAs. We have validated WBRT for the propagation of a coherent field through an aperture and a single lens but expect the method to hold for any combination of paraxial lenses, mirrors, and multiple apertures. As has been stated before, the effect of paraxial systems (i.e., systems for which all wavefronts, propagators, and optical surfaces are approximated by quadratic functions) on the WDF is a coordinate transformation,[9] which is implemented in WBRT by ray tracing. Therefore, WBRT in the paraxial limit can be seen as the Monte Carlo integration method of paraxial wave optical propagators. For the Fresnel propagator, for instance, this equivalence was shown both numerically and analytically.[14]

Interestingly, our results show that WBRT produces accurate results for thick lenses with NAs up to at least 0.2 (see Fig. 2) and for thin lenses with NAs as high as 0.45 (see Fig. 6). The quadratic approximation of paraxial optics is inaccurate at an NA of 0.2 and clearly violated at an NA of 0.45. It thus appears that WBRT can be used for the simulation of systems beyond the paraxial limit, if they are free of aberrations.

An advantage of WBRT is that the WDF can easily be adjusted for the representation of spatially partially coherent light. The WDF can be defined in terms of the mutual coherence function by replacing the product of the fields at the positions $x + x'/2$ and $x - x'/2$ in Eq. (1), by their correlation over time.[6,9] A question that deserves a separate research (inspired by work of Alonso[23]) is whether the negative intensities observed in WBRT in the presence of aberrations are less pronounced for partially coherent fields. Compared to numerical implementations of paraxial wave propagation methods (i.e., the Collins integral[24]), WBRT has a relatively high computational demand but an extremely low memory usage, which makes it very suited for parallel computing. Simulation times can be significantly reduced by using importance sampling and performing calculations on the GPU.[13]

5 Conclusions

We have implemented a Wigner-based ray tracing tool for diffraction calculations. The WDF of the input field is sampled using a Monte Carlo algorithm, the effect of lenses is assumed to be the coordinate transformations encountered in geometrical optics, and apertures are treated using the Kirchhoff boundary conditions. Our simulations lead to the conclusion that aberration-free systems with moderate NAs can be modeled correctly. In the presence of aberrations or large NAs, the assumption that the propagation can be modeled by coordinate transformations, breaks down dramatically.

This limits the domain of validity of WBRT to simulations in and near the paraxial domain.

References

1. J. B. Keller, "Geometrical theory of diffraction," *J. Opt. Soc. Am.* **52**, 116–130 (1962).
2. A. W. Greynolds, "Propagation of generally astigmatic Gaussian beams along skew ray paths," *Proc. SPIE* **0560**, 33–51 (1986).
3. B. Andreas, G. Mana, and C. Palmisano, "Vectorial ray-based diffraction integral," *J. Opt. Soc. Am. A* **32**(8), 1403–1424 (2015).
4. M. Mout et al., "Simulating multiple diffraction in imaging systems using a path integration method," *Appl. Opt.* **55**, 3847–3853 (2016).
5. E. Wigner, "On the quantum correction for thermodynamic equilibrium," *Phys. Rev.* **40**, 749–759 (1932).
6. M. A. Alonso, "Wigner functions in optics: describing beams as ray bundles and pulses as particle ensembles," *Adv. Opt. Photonics* **3**, 272–365 (2011).
7. L. Dolin, "Beam description of weakly-inhomogeneous wave fields," *Izv. Vyssh. Uchebn. Zaved., Radiofiz.* **7**(3), 559–562 (1964).
8. A. Walther, "Radiometry and coherence," *J. Opt. Soc. Am.* **58**(9), 1256–1259 (1968).
9. M. J. Bastiaans, "The Wigner distribution function applied to optical signals and systems," *Opt. Commun.* **25**, 26–30 (1978).
10. S. B. Oh et al., "Rendering wave effects with augmented light field," *Comput. Graphics Forum* **29**(2), 507–516 (2010).
11. T. Cuypers et al., "Interactive point spread function simulation with diffraction and interference effects," in *Proc. of the Int. Conf. on Imaging Theory and Applications and Int. Conf. on Information Visualization Theory and Applications*, pp. 19–24, (2011).
12. T. Cuypers et al., "Validity of Wigner distribution function for ray-based imaging," in *Proc. of IEEE Int. Conf. on Computational Photography*, pp. 1–9, IEEE, Pittsburgh (2011).
13. T. Cuypers et al., "Reflectance model for diffraction," *ACM Trans. Graphics* **31**(5), 122 (2012).
14. B. M. Mout et al., "A Wigner-based ray-tracing method for imaging simulations," *Proc. SPIE* **9630**, 96300Z (2015).
15. W. D. Furlan et al., "Assessment of a Wigner-distribution-function-based method to compute the polychromatic axial response given by an aberrated optical system," *Opt. Eng.* **42**(3), 753–758 (2003).
16. J. G. Goodman, *Introduction to Fourier Optics*, p. 44, Roberts & Company, Englewood (2005).
17. M. J. Bastiaans and P. G. J. van de Mortel, "Wigner distribution function of a circular aperture," *J. Opt. Soc. Am. A* **13**(8), 1698–1703 (1996).
18. J. J. Stamnes, *Waves in Focal Regions: Propagation, Diffraction and Focusing of Light, Sound and Water Waves*, Taylor & Francis, New York (1986).
19. J. G. Goodman, *Introduction to Fourier Optics*, p. 76, Roberts & Company, Englewood (2005).
20. A. W. Lohmann, J. Ojeda-Castañeda, and N. Streibl, "The influence of wave aberrations on the Wigner distribution," *Opt. Appl.* **13**(4), 465–471 (1983).
21. K. Brenner and A. Lohmann, "Wigner distribution function display of complex 1d signals," *Opt. Commun.* **42**(5), 310–314 (1982).
22. D. Dragoman, "Wigner distribution function applied to third-order aberrations," *Appl. Opt.* **35**(1), 161–168 (1996).
23. M. A. Alonso, "Diffraction of paraxial partially coherent fields by planar obstacles in the Wigner representation," *J. Opt. Soc. Am. A* **26**, 1588–1597 (2009).
24. S. A. Collins, Jr., "Lens-system diffraction integral written in terms of matrix optics," *J. Opt. Soc. Am.* **60**(9), 1168–1177 (1970).

Marco Mout is a PhD candidate at Delft University of Technology (TUD) and a researcher at the corporate research and technology center of the Carl Zeiss AG. He concluded a BSc in mechanical engineering at the TUD in 2009 and obtained an MSc degree in applied physics in 2013 at the same institute. His current research focuses on ray-based diffraction simulations.

Michael Wick studied physics at the Julius Maximilian University of Würzburg and the Technical University of Munich. He holds a PhD in theoretical physics from the latter. In 2011, he joined the corporate research and technology center of the Carl Zeiss AG. He became professor for physics at the Coburg University of Applied Sciences in 2016. His research interests include optical simulation, sensors, and computational imaging.

Florian Bociort holds a PhD in physics from the Technical University of Berlin, Germany. His research interests in the optics group at Delft University of Technology include optimization and optical system design. He is also interested in optics education.

Joerg Petschulat studied physics at Technical University in Chemnitz and Friedrich Schiller University Jena. At the latter, he received his diploma. In 2011, he successfully accomplished his conferral of a doctorate (Dr. rer. nat.) in physics. Between 2011 and 2017, he was working at Corporate Research Center of the Carl Zeiss AG. From 2014, he was director of the system simulation group and, since 2016, director of algorithm development. Today, he is working as the head of global R&D at the Semiconductor Mask Solutions business unit, being a part of the Carl Zeiss SMT GmbH (Semiconductor Manufacturing Technology).

Paul Urbach obtained his PhD from Groningen University and joined Philips Research Laboratory in 1986. In 2000, he was appointed as a professor in diffraction optics and in 2008, as a professor in optics and leader of the Optics Research Group at Delft University of Technology in the Netherlands. His main interests are imaging using polarization, optimization of focused fields, and phase sensitive methods. He is scientific director of the Dutch Optics Centre and president of the European Optical Society.